Impact ignition and combustion of micron-scale aluminum particles pre-stressed with different quenching rates

Kevin J. Hill, Nobumichi Tamura, Valery I. Levitas, and Michelle L. Pantoya

Impact ignition and combustion of micron-scale aluminum particles pre-stressed with different quenching rates

Kevin J. Hill,[1] Nobumichi Tamura,[2] Valery I. Levitas,[3,4] and Michelle L. Pantoya[1]

[1]*Department of Mechanical Engineering, Texas Tech University, Lubbock, Texas 79409, USA*
[2]*Advanced Light Source, Lawrence Berkeley National Laboratory, Berkeley, California 94720, USA*
[3]*Departments of Aerospace Engineering, Mechanical Engineering, and Materials Science and Engineering, Iowa State University, Ames, Iowa 50011, USA*
[4]*Ames Laboratory, Division of Materials Science and Engineering, Ames, Iowa 50011, USA*

Pre-stressing aluminum (Al) particles by annealing and quenching alters dilatational strain and is linked to increased particle reactivity. The quenching rate associated with pre-stressing is a key parameter affecting the final stress state within the Al particle, with faster quenching rates theoretically favoring a higher, more desirable stress state. Micron scale Al particles are annealed to 573 K, then quenched at different rates (i.e., 200 and 900 K/min), mixed with bismuth oxide (Bi_2O_3), and the $Al + Bi_2O_3$ mixtures are examined under low-velocity, drop-weight impact conditions. Both quenching rates showed increased impact ignition sensitivity (i.e., between 83% and 89% decrease in ignition energy). However, the slower quenching rate showed a 100% increase in pressurization rate compared to untreated particles, while the faster quenching rate showed a 97% increase in peak pressure, indicating that these two quenching rates affect Al particles differently. Surprisingly, synchrotron X-ray diffraction data show that the 200 K/min quenched particles have a higher dilatational strain than the untreated particles or the 900 K/min quenched particles. Results are rationalized with the help of a simple mechanical model that takes into account elastic stresses, creep in the alumina shell, and delamination of shell from the core. The model predicts that Al powder quenched at 200 K/min did not experience delamination. In contrast, Al quenched at 900 K/min did not have creep but does have delamination, and under impact, delamination led to major fracture, greater oxygen access to the core, and significant promotion of reaction. Thus, the increase in quenching rate and shell-core delamination are more important for the increase in Al reactivity than pre-stressing alone. *Published by AIP Publishing.* https://doi.org/10.1063/1.5044546

I. INTRODUCTION

Micron scale aluminum (Al) powder is used as a fuel in a variety of applications ranging from pyrotechnics to rocket motors but tends to release energy slowly due to an alumina (Al_2O_3) passivation shell limiting diffusion kinetics. However, a large energy density (i.e., 85 GJ/m^3) makes Al an attractive solution for limited volume applications, and significant study has been conducted to improve Al powder combustion. This paper continues the study of a promising method to enhance the oxidation reaction of micron scale Al powder, namely, the method of pre-stressing.

Pre-stressing is defined here as the intentional creation of permanent stresses in a powder for the purpose of altering the mechanical properties of the core-shell particle and thereby affecting reactivity. Based on the melt dispersion mechanism (MDM) theory,[1,2] compressive stress in the oxide shell delays shell fracture caused by a pressure increase from Al melting in the core. Eventually pressure increases within the core and causes spallation of the shell and aerosolization of the core (via a rarefaction wave), and increases reaction rates and energy release. Some experimental studies[2–4] show quantitative agreement with predictions of MDM. In order to further improve the reactivity of Al particles, compressive stress in the shell should be increased. One of the easiest ways to increase compressive stress in the shell is by annealing and quenching Al particles. Annealing to an elevated temperature for a sufficiently long time[5–7]

allows the stresses induced from manufacture to relax in the Al particles.[8] Rapid quenching to room temperature prevents the core and shell from relaxing back to the pre-annealed state, and the large difference between thermal expansion coefficients [i.e., 23×10^{-6} K^{-1} for Al versus 5×10^{-6} K^{-1} for Al_2O_3 (Refs. 9 and 10)] causes compressive stress to develop in the shell and tensile stress to develop in the core. This change in stress state is linked to changes in reactivity.[11–14]

In order to quantify the stress state within pre-stressed (PS) Al particles, several studies measure dilatational strain within the core[11–14] (e.g., the shell is amorphous, and the strain cannot be directly measured via X-ray diffraction). The primary diagnostic to resolve dilatational strain in the Al particle core-shell structure is synchrotron X-ray diffraction (XRD) using the combined white and monochromatic microbeam approach at the Advanced Light Source (ALS)[15] Particles annealed to 573 K (300 °C) and quenched at moderate rates (i.e., <100 K/min) led to a significant increase in dilatational strain, corresponding to a tensile stress in the Al core and compressive stress in the Al_2O_3 shell.[11–14] However, quench rates approaching those in metallurgical processing are high (i.e., >1000 °C/min) and have not been examined for Al powders.

Additionally, most reactivity characterization on pre-stressed Al particles focuses on thermal initiation.[3,4,11–13] Little work on pre-stressed Al particles[16] has been conducted

for different initiation mechanisms. Impact initiation more closely resembles the potential initiation conditions in kinetic weaponry and missile warheads. While significant research has been conducted on Al initiation at various impact velocity regimes,[17–20] impact ignition has not been used to study pre-stressed micron scale aluminum powder.

The objective of this paper is to examine the influence of faster quenching rates on Al pre-stressing and impact ignition and combustion. The objective will be realized by annealing and quenching Al powder at prescribed rates (using a custom quenching chamber), mixing Al with bismuth oxide (Bi_2O_3),[21] and examining impact ignition using a custom drop weight impact-ignition chamber. Only micron scale Al powders are examined, and their internal stress states are characterized using synchrotron XRD. Impact ignition energy levels and pressurization data are related to total energy deposition into the chamber, and analytical modeling is included to mechanistically explain the results.

II. EXPERIMENTAL

A. Aluminum pre-stressing

The micron-scale aluminum (μAl) powder has a 3–4.5 μm average diameter size distribution and is supplied by Alfa Aesar (Ward Hill, MA). The powder consists of spherical particles with a 4 nm amorphous aluminum oxide (Al_2O_3) shell that inherently passivates the Al core from a spontaneous reaction with oxygen in the environment. The μAl powder is 98 wt. % Al and 2 wt. % Al_2O_3.

The pre-stressed aluminum (PS Al) powder is annealed in a controlled thermal environment using a Q800 DMA (Dynamic Mechanical Analyzer) from TA Instruments. Heating is performed in an air atmosphere with a heating rate of 10 K/min to 573 K (300 °C) and held for 15 min. The DMA cools with liquid nitrogen modeling lump capacitance cooling and programmed at an exponential rate to 298 K (25 °C) according to Eq. (1) with $A = 0.0078$ s^{-1}, $T_a = 298$ (25 °C), $T_0 = 573$ K (300 °C), and t is time in seconds

$$T = T_a + (T_0 - T_a) \exp(-At). \tag{1}$$

In contrast, the super-quenched aluminum (SQ Al) is annealed and quenched in a custom-built chamber shown in Fig. 1 and designed to withstand high thermal gradients

associated with rapid quenching. The powder chamber cools through immersion in a liquid solution composed of water, salt, dish soap, and commercial surfactants. Water has a high heat capacity (4.187 kJ/kgK at 288 K, 15 °C) but added salt decreases the heat capacity (i.e., adding 5 wt. % salt to water reduces the heat capacity by 7%). Dish soap inhibits boiling and reduces surface tension of the mixture, while the surfactant improves wetting and thus heat transfer. The powder chamber is sealed with a high temperature silicone O-ring and contains a K-type thermocouple to directly measure the temperature of the powder throughout annealing and quenching. The liquid solution is composed of 78.6 wt. % water, 9.4 wt. % NaCl, 4.1 wt. % Dawn^{TM} blue dish soap, and 7.9 wt. % Simple Green^{TM}. The exponential quench rate applied to the SQ particles is also governed by Eq. (1), where $A = 0.083$ s^{-1}, $T_a = 298$ (25 °C), and $T_0 = 573$ K (300 °C), an order of magnitude faster than the quenching rate of the DMA. Figure 2 shows a graphical comparison of temperature measurements during quenching for the two quenching procedures outlined above.

B. Mixture preparation

The PS Al, SQ Al, and untreated Al (UN Al) are mixed with spherical 90–200 nm diameter size distribution bismuth oxide (Bi_2O_3) particles from Sigma Aldrich (St. Louis, MO) at an equivalence ratio of 1.3 (all samples were prepared for this slightly fuel rich stoichiometry). The stoichiometric ratio was calculated according to the chemical equation $2Al + Bi_2O_3 \rightarrow Al_2O_3 + 2Bi$. Aluminum comprised 13.2 wt. % of the mixture, and Bi_2O_3 comprised 86.8 wt. % of the mixture, compared to a stoichiometric mixture of 10.5 wt. % Al to 89.5 wt. % Bi_2O_3. The powder is mixed using an acetone carrier fluid, and the slurries are sonicated in a Misonix Sonicator 3000 for 2 minutes in a programmed cycle of 10 s on/off to prevent thermal energy buildup during mixing. All mixtures are prepared using the same procedure. The suspensions are placed in a Pyrex® dish and allowed to dry for 24 h in a fume hood. Upon retrieval, all samples are sieved through 325 mesh using a grounded brush to break up large powder agglomerates.
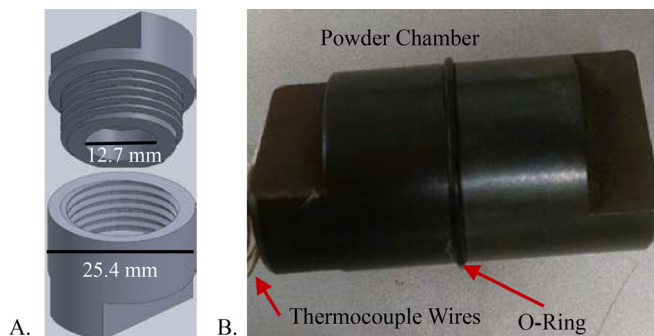

FIG. 1. (a) Schematic of screw powder chamber with 1 g of powder capacity. (b) Photograph of powder chamber including O-ring seal and thermocouple wires.
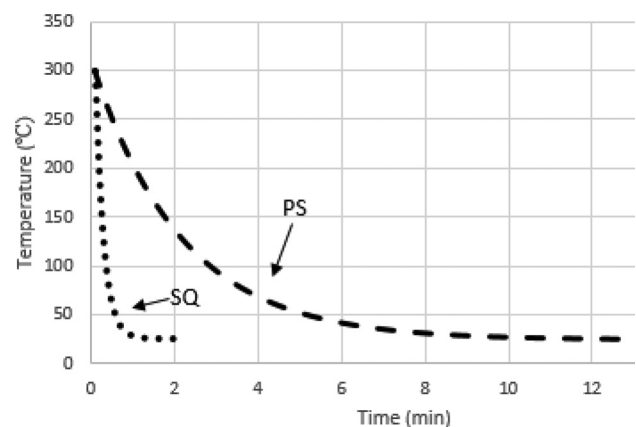

FIG. 2. Temperature history during quenching for PS Al (long dashed line) and SQ Al (short dashed line). Note the linearity associated with SQ Al.

C. Drop weight impact tester

The impact tester has been described previously[16] but is summarized here. Impact is from a carriage that rides on ball bearing pillow blocks running along guide rails with an attached steel striker to impact the intermediate weight on a pressure cell. The pressure cell houses the sample and enables more than just analysis of ignition but also overall reaction energy generation. The maximum energy that can be delivered by the striker carriage is 42 J and is controlled by the drop height and carriage weight—both are adjustable. Instrumentation in the pressure cell to characterize the combustion event includes a photodiode and a pressure sensor (PCB 101A06). The photodiode embedded in the pressure cell enables a "go, no-go" characterization of the ignition event, while the pressure sensor records a pressure-time history within the cell, giving insight into combustion rate and completeness of reaction. Data are recorded at 100 000 samples per second.

D. Experimental setup

Powder samples are loaded into the pressure cell using a low friction polymer plunger to eliminate sample loss through sticking to the plunger. The final powder measured 4.5 mm diameter by 2 mm high with a mass of 10 mg. The loose powder is positioned onto round pieces of course emery cloth in the center of the anvil in the pressure cell, and an intermediate weight is placed on top of the powder sample (i.e., rod on anvil setup); this arrangement is illustrated on the left side of the schematic in Fig. 3. The anvil has a diameter of 10 mm and the emery cloth was cut to match. The carriage height is set, and a pull pin is used to drop the carriage down the rails. No carriage catch is needed because the pressure sensor and high-speed camera (triggered simultaneously) measure when the carriage strikes the intermediate weight. Multiple heights, weights, and sample masses are tested to determine the energy level that would cause ignition, and this approach is called the Bruceton method.[16] The
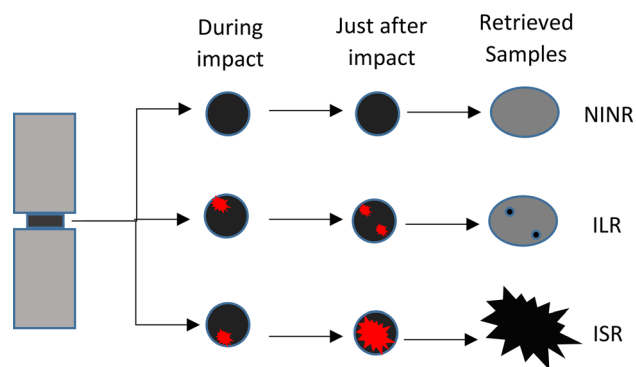

FIG. 3. Schematic representation of impact initiation events. Two anvils compress powder mixture upon impact and sample responses are shown in circular diagrams on the right. During impact, as the anvils move together, local reactions occur (red spots). Just after impact, the local reactions can either propagate or shrink. Upon retrieval, samples that did not fully react have grown radially to a diameter of 10 mm (the same as the anvil) and compressed (thinner as impact energy increases). ILR events demonstrate small black regions (small black spots) from local reactions. ISR events leave nothing visible behind but reaction products.

energy level is increased or decreased based on the results of the previous impact experiments (i.e., how many ignition events occur), and the ignition threshold is defined as the level at which one sample in ten ignites (i.e., Bruceton method[16]) Light emission intensity and pressure as a function of time are collected for all tests, along with high speed video of the falling carriage to quantify impact velocity.

E. XRD characterization

Synchrotron X-ray diffraction (XRD) experiments are performed at the Advanced Light Source facility at Lawrence Berkeley National Laboratory on beamline 12.3.2 using a micron focused synchrotron X-ray beam. Measurements from this beamline that quantify dilatational strain from μAl powder subjected to various annealing and quenching treatments is previously reported.[4,11–13] In a similar procedure,[4,11–13] glass slides are coated with μAl powder and scanned under the X-ray beam (either polychromatic or monochromatic) while a diffraction pattern is collected at each step using a DECTRIS Pilatus 1 M detector. While the polychromatic (Laue) patterns provide the shear components of the strain, the measurement of energy of one indexed reflection provides the missing dilatational component. Data are processed using XMAS software.[22,23] Details of the experimental setup for dilatational strain measurements and synchrotron XRD capabilities are described elsewhere.[22,23]

F. FIB-TEM

Untreated and PS Al particles were milled down with a focused ion beam (FIB) and then examined using a transmission electron microscopy (TEM) to examine grain and grain boundary size and morphology. The FIB system used was a Hitachi NM5000 dual-beam focused ion and electron beam system. The process involves thinning down large ($\sim$10 μm) Al particles down to $\sim$100 nm slices, then transferring the thin slices to a Hitachi H-9500 high resolution TEM for imaging. The process has been described previously in Ref. 12.

III. RESULTS

A. Impact ignition

The samples demonstrate three different responses to impact: (1) no ignition and no reaction (NINR); (2) ignition and limited reaction (ILR); and (3) ignition and significant reaction (ISR); and these are schematically illustrated in Fig. 2. In *Response (1)*, NINR events demonstrate no light emission and no pressurization, while in *Response (2)*, ILR events demonstrate pressure traces with small local increases, but no reaction propagation, and, in *Response (3)*, ISR events show a defined peak pressure and pressurization rate with exponential decay. Table I shows the minimum energy levels required for both significant (ISR) and limited reaction (ILR) events. The term BME (i.e., below minimum energy) is used when the minimum energy for ignition is below the minimum energy of the impact tester. The three responses are identical to previous work[16] using nanoscale powders of aluminum mixed with copper oxide, indicating similarities in ignition and propagation under impact loading owing to pre-stressing.

TABLE I. Minimum energy required (E_{ign}) for ignition and significant reaction (ISR) and ignition and limited reaction (ILR) for PS Al, SQ Al, and UN Al (mixed with Bi_2O_3).

Material	E_{ign} (J/mg) ISR	E_{ign} (J/mg) ILR
UN Al + Bi_2O_3	4.2	1.0
PS Al + Bi_2O_3	0.7	0.5
SQ Al + Bi_2O_3	0.5	BME

Samples of Al were also impacted without oxidizer to examine combustion with atmospheric oxygen, but ignition proved impossible at energy levels up to 42 J.

B. Pressure measurements

Pressure histories are examined for peak pressure, pressurization rate (i.e., representative of reaction rate), and the pressure-time integral (i.e., representative of the extent and duration of combustion). Figure 4 shows three characteristic curves (representing single combustion events) corresponding to UN Al+ Bi_2O_3, PS Al+ Bi_2O_3, and SQ Al+ Bi_2O_3 pressure histories for the ISR (*Response 3*) impact energy level, and Fig. 5 shows the pressure history up to 1 ms during combustion to better illustrate initial pressurization. The data in Figs. 4 and 5 have been filtered using a 100th order low pass filter with a cutoff frequency of 10 kHz to eliminate ringing associated with the pressure chamber. At least three ISR events were recorded for each heating rate (including the untreated samples, and data comparing the distinct pressure responses for the three samples are shown in Table II. Peak pressure is the maximum pressure reached during combustion, pressurization rate is the initial linear rate of pressure increase from the start of combustion to the first local maximum in the event, and the pressure time integral is the numerically integrated area (using the trapezoid rule at each time step) under each curve from the beginning of combustion to the point where pressure returns to atmospheric. Higher peak pressures are observed for the SQ Al+ Bi_2O_3 as well as increased duration of pressure rise time. For example,
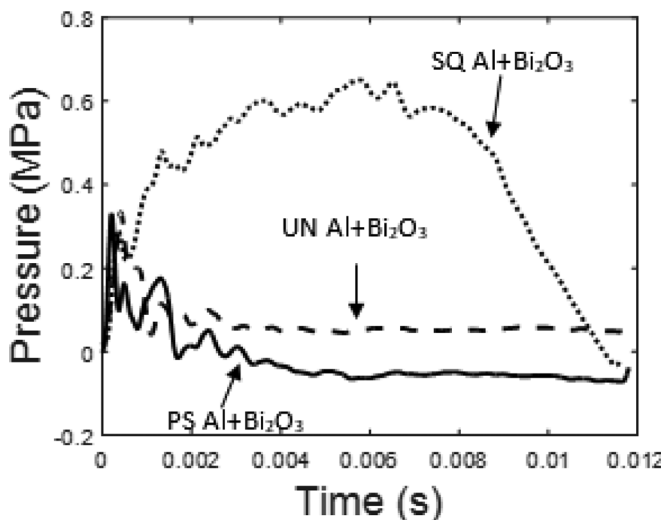

FIG. 4. Comparative pressurization curves for the UN Al+ Bi_2O_3, PS Al+ Bi_2O_3, and SQ Al+ Bi_2O_3 samples at the ISR impact energy level shown in Table I.
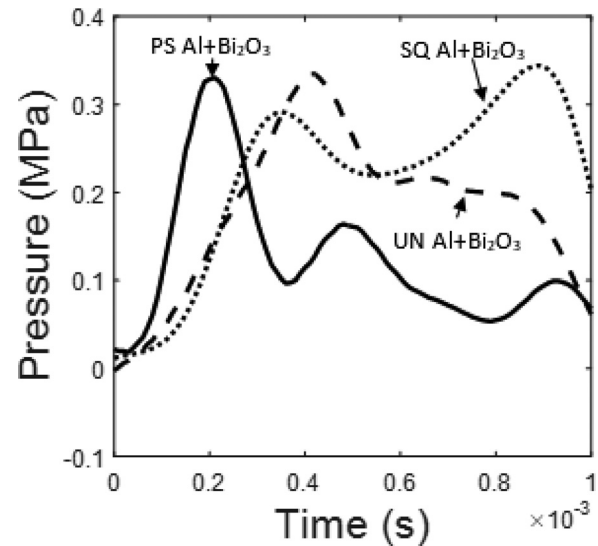

FIG. 5. Comparative pressurization curves for the UN Al+ Bi_2O_3, PS Al+ Bi_2O_3, and SQ Al+ Bi_2O_3 samples at the ISR impact energy level shown in Table I, up to 1 ms during the combustion event.

peak pressure occurs at 6 ms for SQ Al + Bi_2O_3 and less than 1 ms for PS Al + Bi_2O_3 and UN Al + Bi_2O_3. Figure 4 shows that the duration of reaction for SQ Al + Bi_2O_3 is nearly 6 times longer than the other materials with nearly double the peak pressure implying greater gas generation during reaction and more complete combustion, whereas the PS Al + Bi_2O_3 and UN Al + Bi_2O_3 show a sharp initial pressure rise, but within 1 ms the pressure drops. For UN Al + Bi_2O_3 the pressure drops at 1.7 ms but for PS Al + Bi_2O_3, pressure fluctuates to 2 ms. The SQ Al + Bi_2O_3 exhibits nearly identical pressurization rate as the untreated sample, but PS Al + Bi_2O_3 exhibits a nearly double increase in the pressurization rate compared to the other samples. Also interesting is the dramatic increase in pressure-time integral for SQ Al + Bi_2O_3 (consistent with the longer duration of pressure rise) compared to the other samples. The unique differences in reactivity shown through pressure histories imply that different reaction mechanisms may result from varying quenching rates during pre-stressing treatments.

C. Synchrotron X-ray diffraction analysis

Table III shows the average measured dilatational strain for each sample. Note the order of magnitude increase in dilatational strain for pre-stressed materials regardless of quench rate. Interestingly, the SQ Al dilatational strain is measurably smaller than the PS Al.

TABLE II. Peak pressure, pressure-time integral, and pressurization rate data for the UN Al+ Bi_2O_3, PS Al+ Bi_2O_3, and SQ Al+ Bi_2O_3 at the ISR impact energy level for the Taylor rod-on-anvil setup. Standard deviations are shown for each measurement.

Material	Peak pressure (MPa)	Pressure curve area (kPa s)	Pressurization rate (MPa/ms)
UN Al+ Bi_2O_3	0.33 ± 0.1	0.21 ± 0.1	0.80 ± 0.05
PS Al+ Bi_2O_3	0.33 ± 0.1	0.21 ± 0.1	1.57 ± 0.05
SQ Al+ Bi_2O_3	0.65 ± 0.2	5.1 ± 0.5	0.80 ± 0.05

TABLE III. Average dilatational strain in Al powder measured using synchrotron XRD (UN Al and PS Al from Ref. 12). The uncertainty in the strain measurement is $\pm 0.10 \times 10^{-5}$.[11]

Material	Dilatational strain
UN Al	1.5×10^{-6}
PS Al	9.23×10^{-5}
SQ Al	5.7×10^{-5}

D. Total energy release

Using the method developed by Ames,[17] the total energy deposited into a quasi-static chamber of constant volume is shown as follows:

$$\Delta E = \frac{V}{\gamma - 1} \Delta P. \tag{2}$$

In Eq. (2), ΔE is the change in energy of the system, V is the volume of the system, γ is the ratio of specific heats of the gas in the system, and ΔP is the change in pressure (i.e., initial to peak pressure). Table IV shows the energy deposited into the system calculated using Eq. (2) with the assumption that γ is 1.4 (i.e., assuming properties are essentially unchanged by gas generation of the sample and before large temperature changes occur). The chamber volume is $1.75 \, \text{cm}^3$ and ΔP is calculated from Fig. 4.

E. FIB-TEM microstructural analysis

Untreated and PS Al particles were examined using a focused ion beam (FIB) to slice an electron transparency thickness sample from a $10 \, \mu\text{m}$ diameter Al particle. The Al slice was then analyzed using Transmission Electron Microscopy (TEM) to image the internal crystalline Al grains (SQ Al will be examined in future work). Two images shown in Fig. 6 compare grain structure and grain boundaries. The images were taken at an accelerating voltage of 300 kV and a direct magnification of 8000×.

IV. MODELING

In order to rationalize the experimental results and estimate parameters, like the critical stress for delamination, σ_{cd}, the hoop creep strain in an alumina shell, ε_c^h, and the degree of delamination of the shell from the core, d, we developed a simplified model. We will evaluate the stress-strain state of the Al core–Al$_2$O$_3$ shell particle using a generalization of the model in Ref. 13 to take into account delamination

$$\sigma_h = -\frac{18(\varepsilon_2^T - \varepsilon_1^T + \varepsilon_c^h)G_2 K_1 K_2}{(3K_2 + 4G_2)K_1}(1 - d), \tag{3}$$

TABLE IV. Calculated energy deposition into the system per gram of thermite using Eq. (2).

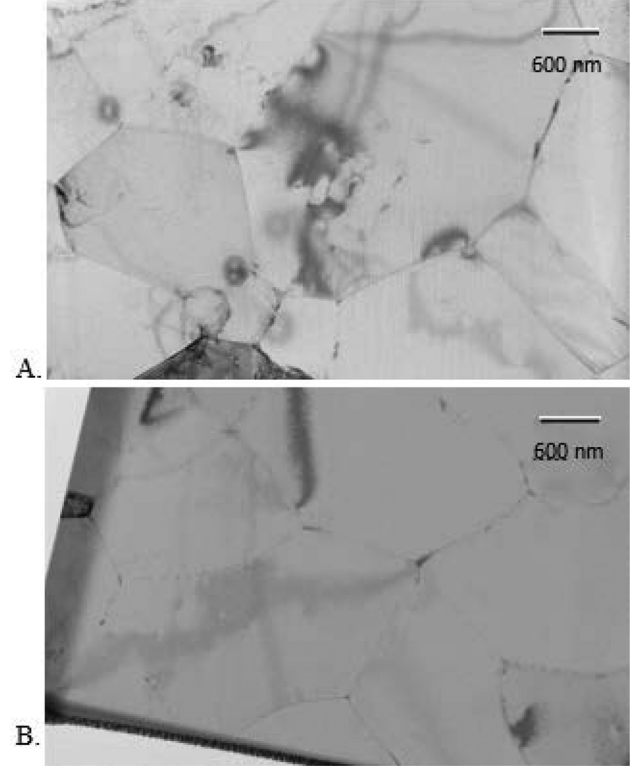| Material	Energy deposited (J/g)
UN Al+ Bi$_2$O$_3$	144.4 ± 40
PS Al+ Bi$_2$O$_3$	144.4 ± 40
SQ Al+ Bi$_2$O$_3$	284.4 ± 80

FIG. 6. TEM images for the grain structure and boundaries of a slice from (a). UN Al particle; and (b) PS Al particle.

$$\sigma_0 = -\frac{2\sigma_h}{M} = \frac{36(\varepsilon_2^T - \varepsilon_1^T + \varepsilon_c^h)G_2 K_1 K_2}{M(3K_2 + 4G_2)K_1}(1 - d), \tag{4}$$

$$\varepsilon_0 = \frac{\sigma_0}{K_1} = \frac{36(\varepsilon_2^T - \varepsilon_1^T + \varepsilon_c^h)G_2 K_2}{M(3K_2 + 4G_2)K_1}(1 - d), \tag{5}$$

$$\varepsilon_1^T = \alpha_1(T - T_0); \quad \varepsilon_2^T = \alpha_2(T - T_0). \tag{6}$$

Here, σ_h is the hoop stress in the alumina shell, σ_0 is the mean stress (negative pressure) in the alumina core, ε_0 is the dilatational strain in the core (which is measured in the current paper), subscripts 1 and 2 designate the Al core and the Al$_2$O$_3$ shell, respectively, α is the linear thermal expansion coefficient, G and K are shear and bulk moduli, $M = R/\delta$ (with the alumina shell thickness δ and the particle core radius R), ε^T is the thermal strain, T is the particle temperature, and T_0 is the temperature at which the core-shell system is stress-free. The damage parameter d characterizes in a simplified averaged way the degree of delamination of the shell from the core. For $d = 0$, Eqs. (3)–(6) coincide with those in Ref. 13, where delamination is neglected. For $d = 1$, complete delamination occurs, and all stresses are zero. The degree of delamination can be defined as the ratio of the delaminated area to the total area of the particle where core and shell meet. Note that the model in Ref. 13 is a generalization of the model in Refs. 1 and 2 for the case with creep strain. For micron particles, M is in the range 500–2000 (i.e., much larger than unity) which is taken into account in Eqs. (3)–(6). The above stresses are the internal stresses, and we do not consider applied external stresses here.

Let us discuss pre-stressing and stress relaxation based on Eqs. (3)–(6). Consider first $\varepsilon_c^h = 0$ and $d = 0$. If $T = T_0$,

then all stresses are zero, which corresponds to the definition of T_0. Usually, for untreated particles, T_0 coincides with the room temperature, T_r. After heating to some temperature T_a, $T > T_0$, and Eqs. (3)–(6) suggest compressive (negative) mean stress σ_0 in a core and tensile (positive) hoop stress σ_h in a shell, which may lead to fracture in the shell if σ_h exceeds the strength of alumina. Sufficiently long annealing leads to complete stress relaxation and can be reached when the creep strain in the shell is $\varepsilon_c^h = \varepsilon_1^T - \varepsilon_2^T$. It is more convenient and traditional to consider a stress-free particle as a pristine particle with $\varepsilon_c^h = 0$ and a new $T_0 = T_a$, which also results in a stress-free particle at the annealing temperature and corresponds to the definition of T_0. During reduction in temperature (i.e., quenching), $T < T_0$ and the sign of stresses in Eqs. (3)–(6) changes: the mean stress σ_0 is tensile in the core and the hoop stress σ_h is compressive in the shell. The goal of pre-stressing is to keep such stresses as high as possible at room temperature, so that during heating in a flame, tensile stresses in a shell will be smaller, and fracture of the shell will be delayed to higher temperature or applied loading. Thus, ideally stress relaxation during quenching should be avoided, which can be achieved by sufficiently fast cooling. However, if the normal stress at the core-shell interface (equal to σ_0) reaches or exceeds the critical stress for delamination, σ_{cd}, as shown in Eq. (7), then delamination of the shell occurs

$$\sigma_0 \geq \sigma_{cd}. \tag{7}$$

The fact that the dilatational strain after PS under a slower quench rate is higher than the dilatational strain after SQ under a faster quench rate means:

(a) There is partial delamination of the shell from the core during quenching at 900 K/min (SQ Al), which leads to stress relaxation. That means that the criterion in Eq. (7) is met during quenching. We assume that creep does not have time to occur for this cooling rate.
(b) There is stress relaxation due to creep during cooling at 200 K/min (PS Al) and the mean stress does not reach the delamination stress σ_{cd}. If condition in Eq. (7) is met and there is creep, then dilatational strain ε_0 should be smaller than for cooling at 900 K/min. Since it is larger, the delamination condition is not met, which is possible with creep relaxation only.

Substituting values from Table V into Eqs. (4)–(6) for $T_0 = 573$K and $T = 298$K, we obtain the following:

$$\sigma_h = (-2.58 - 525.12\varepsilon_c^h)(1 - d), \tag{8}$$

$$\sigma_0 = \frac{5.170 + 1050.24\varepsilon_c^h}{M}(1 - d), \tag{9}$$

TABLE V. Material parameters for aluminum (subscript 1) and alumina (subscript 2) at room temperature.[15]

K_1 (GPa)	K_2 (GPa)	G_2 (GPa)	α_1 (10^5 K^{-1})	α_2 (10^5 K^{-1})
76	252	163	2.33	0.54

$$\varepsilon_0 = \frac{0.0680 + 13.819\varepsilon_c^h}{M}(1 - d). \tag{10}$$

For 3–4.5 μm average diameter Al powder with an oxide thickness of 4 nm, the range of M is from 375 to 562. However, due to variation of the oxide thickness and particle diameter, we plot in Fig. 7 σ_0 and ε_0 versus M in the range from 300 to 1250 for $d = 0$ and $\varepsilon_c^h = 0$. In this range, dilatational strain varies from 5.4×10^{-5} to 24.7×10^{-5} and mean stress from 0.0041 to 0.0172 GPa. The hoop stress is equal to -2.58 GPa and is independent of M. These are the upper bounds of the magnitude of all parameters when creep and delamination are neglected, and also values of the critical dilatational strain and stress σ_{cd} for delamination. If we assume that averaged $M = 600$, then $\sigma_0 = \sigma_{cd} = 0.009$ GPa and corresponding critical dilatational strain is 11.3×10^{-5}. When cooling at 900 K/min, $\varepsilon_0 = 5.7 \times 10^{-5}$, and substitution in Eq. (10) at $\varepsilon_c^h = 0$ results in the degree of delamination of the shell from the core $d = 0.52$, i.e., more than half of area is delaminated. The corresponding mean stress and hoop stress are $\sigma_0 = 0.004$ GPa and $\sigma_h = -1.25$ GPa. For cooling at 200 K/min, $\varepsilon_0 = 9.23 \times 10^{-5}$; substitution of this strain in Eq. (9) at $d = 0$ results in the creep strain $\varepsilon_c^h = -91.4 \times 10^{-5}$, which is very small but still an order of magnitude larger than ε_0. The corresponding mean stress and hoop stress are $\sigma_0 = 0.007$ GPa and $\sigma_h = -2.10$ GPa.

Thus, based on simplified modeling, it is estimated that:

(a) The critical delamination stress is $\sigma_{cd} = 0.009$ GPa and corresponding critical dilatational strain is 11.3×10^{-5}.
(b) For cooling at 200 K/min the creep strain $\varepsilon_c^h = -91.4 \times 10^{-5}$, the mean stress and hoop stress are $\sigma_0 = 0.007$ GPa and $\sigma_h = -2.10$ GPa, respectively.
(c) For cooling at 900 K/min, the degree of delamination of the shell from the core d $= 0.52$, and the mean stress and hoop stress are $\sigma_0 = 0.004$ GPa and $\sigma_h = -1.25$ GPa, respectively.

V. DISCUSSION

Table I shows the impact energy needed for ISR events of PS Al+ Bi$_2$O$_3$ is 83% less than what is needed for UN Al+ Bi$_2$O$_3$. The impact energy needed for ISR of SQ Al+ Bi$_2$O$_3$ is slightly less than for the PS Al+ Bi$_2$O$_3$ and 88% less than UN Al+ Bi$_2$O$_3$. The impact energy required for ILR events for PS Al+ Bi$_2$O$_3$ is 50% less than UN Al+ Bi$_2$O$_3$, and ILR events are recorded for the SQ Al+ Bi$_2$O$_3$ all the way down to the 0.3 J/mg level, the lowest energy level the impact tester can currently reach. These variations are likely due to changes in particle stress state and delamination of the shell after heat treatment, both are discussed further.

Insight into reactivity can be obtained from the pressure history shown in Figs. 4 and 5. The pressurization rate for PS Al+ Bi$_2$O$_3$ is about twice as high as UN Al+ Bi$_2$O$_3$, but the extent of combustion is significantly higher for SQ Al+ Bi$_2$O$_3$. The pressure curves (Fig. 3) are numerically integrated to examine gas generation, which is indicative of the amount of material consumed during combustion. The
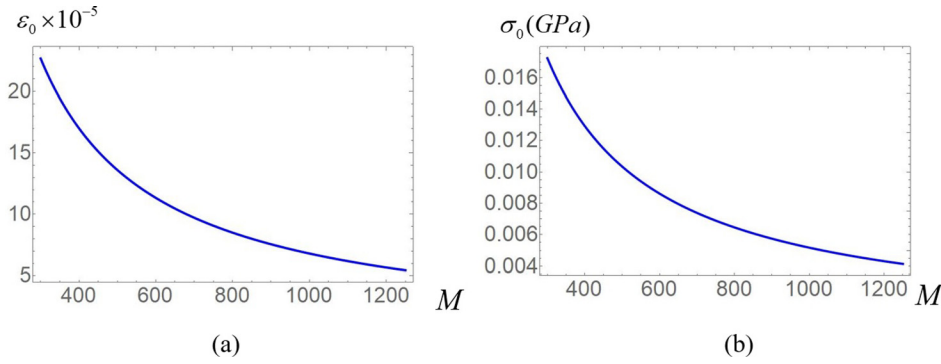
FIG. 7. Dependence of the dilatational strain ε_0 and mean stress σ_0 on the dimensional particle radius $M = R/\delta$ for $d = 0$ and $\varepsilon_c^h = 0$.

integral value of the pressure curve for PS Al+ Bi$_2$O$_3$ is identical to UN Al+ Bi$_2$O$_3$ (Table II) indicating that although the impact sensitivity is much higher for PS Al+ Bi$_2$O$_3$, the amount of combustion is actually quite similar. However, the SQ Al+ Bi$_2$O had a 2300% increase in curve area compared to the UN and PS Al particles, indicating significantly more complete combustion. Table II also shows that PS Al+ Bi$_2$O$_3$ and UN Al+ Bi$_2$O$_3$ exhibit identical peak pressure, but the SQ Al+ Bi$_2$O$_3$ shows peak pressure almost doubled. Pressurization rates are identical for SQ Al+ Bi$_2$O$_3$ and UN Al+ Bi$_2$O$_3$, but the PS Al+ Bi$_2$O$_3$ shows a pressurization rate nearly double. The SQ Al+ Bi$_2$O$_3$ demonstrates significantly more complete combustion during ISR events, but the PS Al+ Bi$_2$O$_3$ shows a higher pressurization rate.

Synchrotron XRD data in Table IV show that there is a measurable increase in dilatational strain in the PS Al and SQ Al particles compared to the UN Al particles. However, the increase is smaller for the SQ Al particles. As discussed above, this is likely due to small local de-laminations of the shell from the core due to the rapid quench rate for SQ Al particles. This observation can also help explain why the pressurization rate of the SQ Al particles is lower than the PS Al particles, but the amount of combustion is considerably higher.

To further examine energy release behavior from impact initiation, the system is analyzed as a quasi-static, constant volume system. Venting effects and heat transfer into the steel cell are not considered and account for significant losses from the ideal adiabatic case. Both the UN Al and PS Al demonstrate similar total energy release (Table IV), while the SQ Al releases nearly double the energy (i.e., about 144 compared with 284 J/g, respectively). Ideal, adiabatic thermal equilibrium simulations using REAL-Code (Timtech L. L. C.)[24] show that the heat of combustion of Al + Bi$_2$O$_3$ is 2032 J/g, far greater than the measured values. The low measured values are probably the result of significant heat conduction into the steel of the impact cell, causing the quasi-static pressure to peak at a lower pressure than in a truly adiabatically isolated cell.

The microstructure of the UN and PS Al samples is examined with FIB-TEM visualization in Fig. 6. Both images are taken at the same accelerating voltage (300 kV). Both images show essentially the same microstructure: large (>600 nm) grains surrounded by well-defined grain boundaries. The morphology of the grains and their boundaries are identical.

The analytical model and results in Fig. 7 enable qualitative discussion of the experimental results. As it is concluded in Sec. IV, PS Al is not subjected to delamination; there is some creep in the shell, and hoop stress is quite high, −2.10 GPa. During heating without mechanical loading, compressive hoop stresses in the shell suppress fracture of the shell due to tensile hoop stress that appears because of the thermal expansion and melting of the aluminum core. For relatively low impact energy, local contact loading of the alumina shell causes local bending and fracture of the shell, opening the bare Al core for oxidation by gaseous oxygen or oxygen from Bi$_2$O$_3$. Small bare Al core areas may heal during reaction before self-supporting oxidation starts. The larger the impact energy and bare area, the higher are the chances that a reaction will be detected as an ignition event. For some critical impact energy and corresponding bare area, the self-supported reaction occurs until limited or significant oxidation. Compressive hoop stress in the shell due to pre-stressing but before delamination should delay fracture of the shell during bending in regions with tensile stresses. At the same time, larger accumulated elastic energy of the internal stresses that is released during fracture leads to larger energy release rates upon fracture as well as larger fractured regions and bare areas of Al. That is why minimum energy required for ISR and ILR is much smaller for PS Al than for UN Al, and pressurization rate is two times larger. However, the peak pressure, pressure-time integral, and deposited energy are the same for PS Al and UN Al. It should be noted that in the experiment comparison is performed for impact energies corresponding to ISR minimum energy levels from the middle column in Table I, i.e., impact energy for PS Al is six times smaller than for UN Al.

SQ Al particles do not have time to accumulate creep strain but have delamination of the shell from the core in slightly more than half of the particle surface, which increases dilatational strain to 5.7×10^{-5} and the hoop stress to −1.25 GPa. If a particle with partially delaminated shell is subjected to impact, there is a much higher probability that cracks will be produced in the shell or break the delaminated part of the shell. In both cases, accessibility of gaseous oxygen strongly increases. That is why minimum energy required for ISR and ILR is much smaller for SQ Al than for UN and PS Al; the peak pressure, pressure-time integral, and deposited energy are significantly larger for SQ Al than for PS Al and UN Al. The counterintuitive result that the pressurization rate for SQ Al is the same for UN Al and two
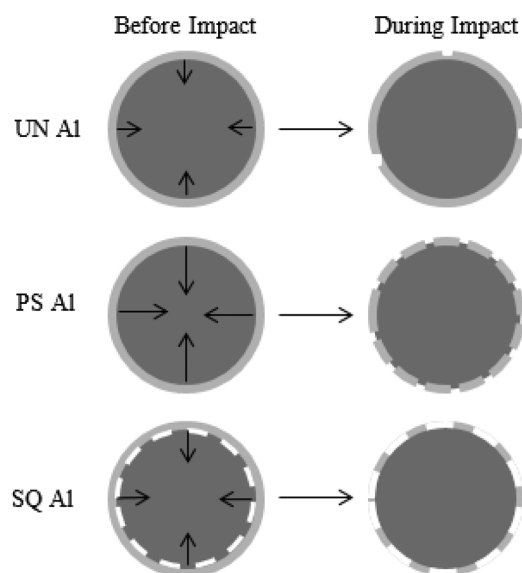
FIG. 8. Schematic representation of reaction mechanism for micron scale particles. The arrows represent the magnitude of internal stress pulling on the shell. Limited shell failure occurs during impact for the UN Al, while significant failure occurs for both PS Al and SQ Al. The area of active aluminum revealed during impact is higher for the SQ Al due to delamination of the shell during quenching.

times smaller than for PS Al can be explained by two opposing effects that are illustrated in Fig. 8. While delamination significantly promotes reaction, comparison of experiments is performed for the impact energies from the last column in Table I, i.e., impact energy for SQ Al is significantly smaller than for UN and PS Al. The proposed reaction mechanism is shown schematically in Fig. 8. The dark grey represents the crystalline aluminum core, and the light grey represents the amorphous alumina shell. The arrows represent the magnitude of stress acting on the core (as calculated using the measured dilatational strain). Prior to impact, both the UN Al and PS Al have shells that are fully adhered to the core. In contrast, the SQ Al exhibits some delamination (represented by the white dashed line). During impact, the level of shell failure in each sample is a function of the stresses in the particles as well as the level of shell delamination. The UN Al demonstrates the least shell failure, as represented by the fewest holes in the shell. The PS Al demonstrates significant spallation of the shell as the stresses relax violently, as represented by the large number of "cracks" in the shell (gaps in the schematic oxide). The SQ Al demonstrates fracture and removal of delaminated parts of the shell as they are the unsupported and weakest parts. Holes in shell during impact correspond to delaminated (white) regions in the scheme before impact.

VI. CONCLUSION

Micron aluminum and bismuth oxide (Al$+$ Bi_2O_3) composites are characterized under low velocity impact as a function of the pre-stressed state of the Al powder. The pre-stressed state of the Al powder was manipulated by varying the quench rate from 200 to 900 K/min corresponding to pre-stressed (PS) and super quenched (SQ) Al. Results show that PS Al leads to 3.5 J/mg reduction in minimum ignition

energy compared to the untreated counterpart and SQ Al leads to a 3.7 J/mg difference in minimum ignition energy. Combustion results showed that the SQ Al burned significantly more completely with an area under the transient pressure curve increase by 2300% compared to untreated samples and nearly double (97% increase) the energy deposition into the impact chamber. The PS Al demonstrated a higher pressurization rate (two times that of the untreated and SQ Al). Synchrotron XRD data show dilatational strain in PS and SQ Al is much larger than in the untreated samples, with the PS Al showing the largest increase in strain. Some microstructural visualization shows that large changes in grain and grain boundary morphology do not occur during annealing and quenching processes. Experimental results are qualitatively rationalized with the help of a simple mechanical model that takes into account elastic stresses, creep in the alumina shell, and delamination of shell from the core. The PS Al most probably did not have delamination but still had some stress relaxation due to creep. In contrast, SQ Al did not have creep but had delamination, which under impact led to major fracture and access of oxygen to the core and significant promotion of reaction in comparison with PS and especially UN samples. Consequently, reaching delamination is more important for increasing particle reactivity than just increasing compressive hoop stresses in the shell. Thus, the increase in the quenching rate is important for activation of alternative mechanisms of stress relaxation and increase Al reactivity.

[1] V. I. Levitas, B. W. Asay, S. F. Son, and M. Pantoya, J. Appl. Phys. **101**, 083524 (2007).
[2] V. I. Levitas, Philos. Trans. R. Soc. A **371**, 20120215 (2013).
[3] B. Dikici, M. L. Pantoya, and V. I. Levitas, Comb. Flame **157**(8), 1581 (2010).
[4] V. I. Levitas, J. McCollum, and M. L. Pantoya, Sci. Rep. **5**, 7879 (2015).
[5] S. Timoshenko, J. Opt. Soc. Am. **11**, 233 (1925).
[6] J. F. Throop, J. H. Underwood, and G. S. Legar, *Residual Stress and Stress Relaxation*, edited by E. Kula and V. Weiss (Plenum Press, 1971).
[7] M. R. James, "Relaxation of residual stresses: An overview," in *Advances in Surface Treatments*, edited by A. Niku-Lari (Pergamon Press, 1987), Vol. IV.
[8] D. A. Firmansyah, K. Sullivan, K.-S. Lee, Y. H. Kim, R. Zahaf, M. R. Zachariah, and D. Lee, J. Phys. Chem. C **116**, 404 (2012).
[9] J. E. Hatch, *Aluminum: Properties and Physical Metallurgy* (American Society for Metals, 1984).
[10] E. Dorre and H. Hubner, *Alumina: Processing, Properties and Applications* (Springer, 2011).
[11] J. McCollum, M. L. Pantoya, and N. Tamura, Acta Mater. **103**, 495 (2016).
[12] J. McCollum, D. K. Smith, K. J. Hill, M. L. Pantoya, J. Warzywoda, and N. Tamura, Comb. Flame **173**, 229 (2016).

[13]V. I. Levitas, J. McCollum, M. L. Pantoya, and N. Tamura, Comb. Flame **170**, 30 (2016).

[14]V. I. Levitas, J. McCollum, M. L. Pantoya, and N. Tamura, J. Appl. Phys. **118**, 094305 (2015).

[15]J. S. Chung and G. E. Ice, J. Appl. Phys. **86**(9), 5249 (1999).

[16]K. J. Hill, J. Warzywoda, M. L. Pantoya, and V. I. Levitas, J. Appl. Phys. **122**, 125102 (2017).

[17]R. G. Ames, in *43rd AIAA Aerospace Sciences Meeting and Exhibit* (2005), p. 279.

[18]J. Hooper, C. L. Milby, R. J. Lee, and R. J. Jouet, Procedia Eng. **58**, 663 (2013).

[19]S. M. Walley, J. E. Field, R. A. Biers, W. G. Proud, D. M. Williamson, and A. P. Jardine, Propellants, Explos., Pyrotech **40**, 351 (2015).

[20]C. S. Coffey and V. F. DeVost, Propellants, Explos., Pyrotech. **20**, 105 (1995).

[21]X. Wang, W. Zhou, J. DeLisio, G. Egan, and M. R. Zachariah, Phys. Chem. Chem. Phys. **19**, 12749 (2017).

[22]M. Kunz, N. Tamura, K. Chen, A. A. MacDowell, R. S. Celestre, M. M. Church, S. Fakra, E. E. Domning, J. M. Glossinger, J. L. Kirschman, G. Y. Morrison, D. W. Plate, B. V. Smith, T. Warwick, H. A. Padmore, E. Ustundag, and V. V. Yashchuk, Rev. Sci. Instrum. **80**, 035108 (2009).

[23]N. Tamura, "XMAS: A versatile tool for analyzing syncrotron x-ray microdiffraction data," in *Strain and Dislocation Gradients from Diffraction: Spacially-Resolved Local Structure and Defects*, edited by R. Barabash and G. Ice (Imperial College Press, 2014), p. 125.

[24]G. V. Belov, Propellants, Explos., Pyrotech. **23**, 86 (1998).